Predictive model for micrometeoroid damage to gossamer structures

Michaela N. Villarreal, Jonathan W. Arenberg,* and Lauren Halvonik Harris
Northrop Grumman Corporation, Redondo Beach, California, United States

Abstract. A typical inflatable reflector for space application consists of two thin membranes with a parabolic shape. It is critical to understand the interaction of the inflatable and the micrometeoroid environment to which it is exposed. This interaction leads to a series of penetrations of the inflatable membrane on the entrance and exit of the impacting particle, creating a pathway for gas to escape. To increase the fidelity of the of the estimated damage that will be incurred, we examine the literature for descriptions of micrometeoroid fragmentation and present a theoretical formulation for the damage caused by an impacting particle to the entrance and exit membranes. This theory is compared with an initial set of hyper-velocity tests for micrometeoroid-sized particles on thin film membranes. We use the results of these tests to produce a predictive model. This model is applied to estimate the damage rate near the 1 AU location and output predictions for the effectiveness of a micrometeoroid shield to reduce the damage on the lenticular and effectively optimize its lifetime. Finally, we apply the kinetic theory of gasses to develop expressions for the expenditure of gas over a specified mission lifetime due to penetrations. Although we examine the specific case of an inflated lenticular protected by extra membrane layers, our predictive model can be applied to any gossamer structure composed of polyimide membranes.
 [DOI: 10.1117/1.JATIS.8.4.044006]

Keywords: gossamer structures; inflatable optics; micrometeoroid fragmentation; inflation control.

Paper 22043G received Apr. 5, 2022; accepted for publication Nov. 16, 2022; published online Dec. 12, 2022.

1 Introduction

This work was inspired by our work on an observatory concept based on inflatable optics.[1] In an earlier era, this class of systems was described by the adjective gossamer. We employ this term to make this work easier to relate to the substantial body of literature that can be found under that key word.

An inflatable reflector is typically composed of two thin sheets (such as Kapton) in a balloon-like structure with a parabolic shape. One side of the structure is aluminized to function as the primary reflector, and the other side is transparent to allow the incoming light to pass. The structure is supported by an inflatant that enables the sheets to take on the proper shape. In 1996, the inflatable antenna experiment was carried out, proving that such a design can be successfully deployed.[2]

Inflatable reflectors offer a direct path to unlock large (>10-m diameter) aperture space telescopes that could not be implementable with a rigid mirror design. These large apertures can significantly advance the current understanding of astrophysics and planetary systems by increasing the signal to noise ratio and the number of targets that can be observed in a given time frame.[3] Hence, maximizing the lifetime of these systems is highly desired.

Inflatable systems have one main vulnerability that limit their lifetimes: micrometeoroid impacts from the space environment create holes in the structure that allow the inflatant to escape. This requires replenishment of the gas to keep the lenticular properly inflated, the mass

*Address all correspondence to Jonathan W. Arenberg, jon.arenberg@ngc.com

requirement for which sharply rises with lifetime (see Sec. 5). Therefore, it is crucial to properly account for how quickly the space environment will create perforations in the inflatable structure.

A previous set of experiments were performed to analyze shape changes in response to pressure change, a thermal gradient, and a controlled puncture for a 1-m inflatable optic.[4] The controlled puncture experiment used a needle with a diameter of 600 μm to simulate a micrometeoroid impact on one side of the reflector. No evidence of tear propagation was observed. The reflector exhibited fluctuations in its surface shape for tens of minutes before re-stabilizing. It is worth noting that the size of the needle diameter corresponded to a fairly large-sized micrometeoroid (see Sec. 4); therefore, the response represents a near worst-case scenario.

The purpose of this paper is to create a predictive model for the damage incurred on an inflatable optic over time due to its local micrometeoroid environment. In Sec. 2, we review the theory for grain fragmentation and present a formulation for how to calculate the total damage from an impacting micrometeoroid. Section 3 covers results from new hypervelocity tests conducted at the White Sands Test Facility (WSTF) to mimic such events. These results are modeled using the formulation from Sec. 2 to determine the empirical values for the relevant parameters and construct a predictive model. This model is then applied to estimate the requirements to compose a structure capable of sufficiently breaking down incoming micrometeoroids so that little to no fragments impact the lenticular. Finally, we identify the gas flow regime for escape through impact holes and derive an expression for the total gas required to replenish the lenticular over a specified mission lifetime.

2 Theoretical Formulation for Micrometeoroid Punctures and Fragmentation

In this section, we review the fundamental physics involved in micrometeoroid impacts.

2.1 *Micrometeoroid Puncture Size on Entrance and Amplification of Damage*

A single micrometeoroid will cause damage to both sides of the inflatable structure as it enters and exits. These damage areas will not be equal; the micrometeoroid will shatter after encountering the first surface, creating many fragments that will subsequently cause many punctures on the exit surface (see Fig. 1). This section focuses on calculating the damage upon the initial

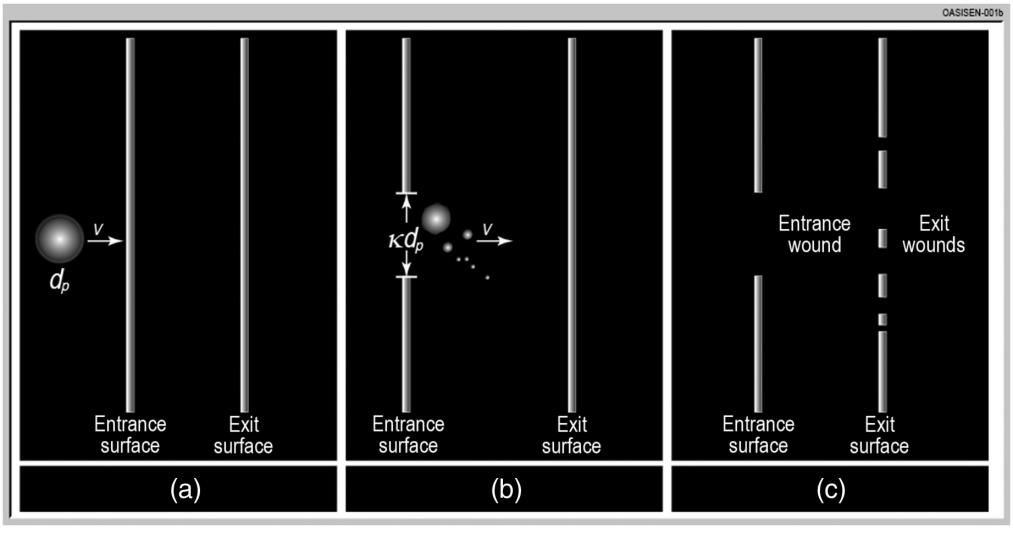

Fig. 1 Schematic of the stages of a micrometeoroid impact. (a) Incoming micrometeoroid impacts the first membrane, creating a single hole. (b) Micrometeoroid shatters after impact, creating a distribution of fragments that impact the second membrane. (c) Resulting damage allows a mechanism for gas escape.

surface. To accomplish this, we first review past literature that established the relationship between impactors and punctures. We then leverage this knowledge to create an expression to estimate the damage for a single impact.

To begin, we first want to understand how the hole size varies with the size of the impactor. We begin our analysis with Gardner et al.,[5] who used hypervelocity tests on thin films to determine an equation that describes how to retrieve an impactor's diameter using the puncture size that it left behind. This was chosen as our starting point because of the similarity with our intended analysis, namely an estimated population of hole sizes on gossamer films. Gardner et al.[5] showed that an impactor's diameter can be inferred from the observed hole diameter with the expression

$$d_p' = \eta\left(\frac{10}{9+\exp(D_h'/\beta)}\right) + D_h'(1-\exp(D_h'/\beta)), \tag{1}$$

where $d_p' = d_p/f$ is the ratio of the projectile diameter d_p to the thickness of the film f, $D_h' = D_h/f$ is the ratio of the hole diameter D_h to the thickness of the film, and η and β are coefficients. The coefficient η is calculated as

$$\eta = 6.97\left(\frac{V\rho_p}{\sqrt{\sigma_t\rho_t}}\right)^{-0.723}\left(\frac{\sigma_t}{\sigma_{Al}}\right)^{-0.217} f^{-0.053}, \tag{2}$$

where V represents the impactor's velocity, ρ_p is the density of the projectile, ρ_t is the density of the target, σ_t is the yield stress of the target, σ_{Al} is the yield stress of aluminum, 6.90×10^7 Pa, and f is the thickness of the film in μm. This equation can be applied using any set of internally consistent units (this is partially accomplished by the presence of σ_{Al} in Eq. 2), with the exception that f and d_p must be in units of μm. It is worth noting that the η coefficient brings in the implicit dependencies of the hole size on the projectiles' properties, such as density and velocity, and on the properties of the membrane, such as its density, thickness, and strength.

The coefficient β is dependent on the impactor's velocity and behaves such that

$$\beta = \beta_1 + \beta_2 V, \tag{3}$$

where β_1 and β_2 are determined empirically for a specific target composition using hypervelocity data with V in units of km/s.

Figure 2 shows the relationship between the projectile diameter d_p and the hole diameter observed D_h for an impacting velocity of 7 km/s and for input values representative of a ruby particle impacting a 0.5 mil Kapton film (this will be the setup for our experiments in Sec. 3). The corresponding inputs are then $f = 12.7$ μm, $\sigma_t = 8.79\times10^7$ Pa, $\rho_t = 1380$ kg/m^3, and $\rho_p = 3950$ kg/m^3. The parameter β is defined as $\beta = 13.3 + 0.55$ V (see Sec. 3.3 for more

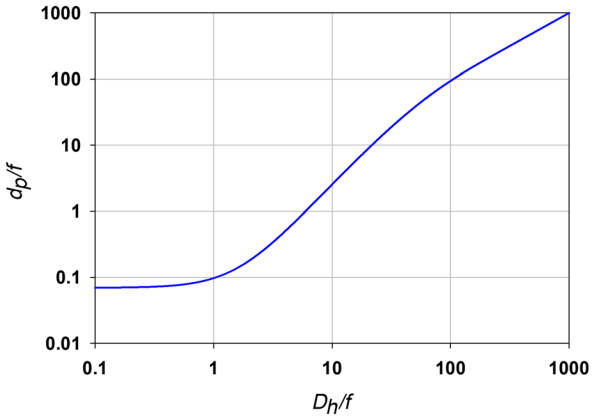

Fig. 2 Equation (1) is plotted for an impacting ruby with a velocity of 7 km/s on 0.5 mil Kapton film. This function is used in Sec. 3.4 to infer the diameters of the fragments, d_f from observed holes.

details). In Sec. 3.4, we apply this function to infer the diameters of impacting fragments that are not known.

Gardner et al.[5] derived Eq. (1) specifically for metallic surfaces. Throughout this paper, we apply this equation for the case of a Kapton (polyimide) membrane. Previous hypervelocity tests on Kapton have shown that it follows a similar overall trend to that derived by Gardner et al.[5] but deviates in shape somewhat in the region between $D_h/f \sim 0.5$ to 4.[6] The purpose of future hypervelocity tests is to obtain enough data to derive a similar function specifically for polyimide films.

Equation (1) is useful for backing out the particle diameter for an observed puncture. However, in this paper, we are interested in the reverse problem: given a particle diameter, what is the corresponding hole diameter? We introduce an amplification factor, κ, that describes the relationship between the particle diameter and the hole size that it creates [for prescribed interaction conditions as defined in Eq. (1)] as

$$\kappa = \frac{D_h}{d_p}. \tag{4}$$

Equation (1) can therefore be used to determine a κ value for a corresponding incoming particle size d_p given a set of input conditions. This involves first mapping d_p to D_h with Eq. (1) and then plugging in these respective values into Eq. (4). Equation (1) reveals that the amplification factor κ at a specific d_p is not constant, but it varies with the properties of the impactor and the film, as well as the relative velocity between the two.

Approximating the micrometeoroid as a spherical grain, the damage area caused to the first membrane (which we refer to as the entrance membrane), A_{ent}, is written as

$$A_{\text{ent}} = \frac{\pi}{\cos\theta}\left(\frac{D_h}{2}\right)^2, \tag{5}$$

$$A_{\text{ent}} = \frac{\pi}{\cos\theta}\left(\frac{\kappa d_p}{2}\right)^2, \tag{6}$$

$$A_{\text{ent}} = \frac{\pi\kappa^2}{4\cos\theta} d_p^2, \tag{7}$$

where θ is the angle of incidence. Therefore, the resulting hole is an ellipse that depends on the angle of incidence.

Gardner et al. [5] also showed that the minimum particle size required to be above the ballistic limit for a given velocity V is found as

$$d_{p,\text{bal}} = \left(\frac{f}{0.129\left(\frac{V\rho_p}{\sqrt{\sigma_t\rho_t}}\right)^{0.763}\left(\frac{\sigma_t}{\sigma_{Al}}\right)^{0.229}}\right)^{1/1.056}, \tag{8}$$

where all terms maintain the same definitions as before. Similar to Eq. (2), this equation is valid as long as all variables are in a consistent set of units, with the exception that f and $d_{p,\text{bal}}$ must be given in μm. We utilize this equation later to determine which micrometeoroids are capable of penetrating the membrane.

2.2 *Micrometeoroid Fragmentation and Puncture Size on Exit*

Micrometeoroids near 1 AU generally impact with velocities of 35 km/s or less.[7] At these impact speeds, the micrometeoroid incident on the entrance membrane will shatter (spalls) into a number of smaller fragments. This collection of fragments will then produce many holes on the exit surface. In this section, we devise an expression for the particle distribution as a result of this fragmentation. We then determine the total damage on the exit membrane due to secondary impacts from these fragments.

We follow the literature for the shattering of interstellar dust grains,[8,9,10] to describe the fragment distribution after the micrometeoroid experiences catastrophic destruction from encountering the first surface. It has been shown that a dust grain that undergoes catastrophic destruction shatters into smaller pieces with a number distribution that is described by a power law,[8,9]

$$n_f(m_f)dm_f = c_f\left(\frac{3m_f}{4\pi\rho}\right)^{-\frac{\alpha_f}{3}} dm_f, \tag{9}$$

where the number distribution of the fragments is denoted by n_f over an interval $(m_f, m_f + dm_f)$ with m_f being the mass of the fragment, c_f is a scaling coefficient, ρ is the mass density, and α_f is the scaling exponent. We assume that the impactor has a uniform density, so the fragments maintain the same density as the original projectile. The literature suggests that α_f is in the range from 3 to 3.5.[8,9,10]

The number distribution is bounded by a minimum and maximum fragment size. The maximum fragment size is believed to be proportional to the projectile radius, a_p, such that[9]

$$a_{f,\max} = c_{\max} a_p, \tag{10}$$

where $a_{f,\max}$ is the radius of the largest fragment and $c_{\max}$ is the scaling coefficient. For the case of catastrophic destruction of the impactor, Jones et al.[9] adopted a value of $c_{\max} = 0.22$, whereas Hirashita and Kobayashi[10] used a value of $c_{\max} = 0.27$. Both applications assume a minimum fragment size $a_{f,\min} \sim 5 \times 10^{-10}$ m as the shattering limit.

We determine c_f by invoking the conservation of mass. The total mass of all fragments must equal the mass of the original particle m_p, and thus

$$m_p = \int_{m_{f,\min}}^{m_{f,\max}} n_f m_f \mathrm{d}m_f. \tag{11}$$

Substituting Eq. (9) into Eq. (11) gives

$$m_p = \int_{m_{f,\min}}^{m_{f,\max}} c_f\left(\frac{3m_f}{4\pi\rho}\right)^{-\frac{\alpha_f}{3}} m_f \mathrm{d}m_f. \tag{12}$$

This simplifies to

$$m_p = c_f\left(\frac{4\pi\rho}{3}\right)^{\frac{\alpha_f}{3}} \int_{m_{f,\min}}^{m_{f,\max}} m_f^{1-\frac{\alpha_f}{3}} \mathrm{d}m_f. \tag{13}$$

This integrates to

$$m_p = \left(\frac{4\pi\rho}{3}\right)^{\frac{\alpha_f}{3}} \frac{c_f}{2-\frac{\alpha_f}{3}} \left(m_{f,\max}^{2-\frac{\alpha_f}{3}} - m_{f,\min}^{2-\frac{\alpha_f}{3}}\right). \tag{14}$$

We rewrite the above equation in terms of the original impactor radius, a_p, and the minimum and maximum fragment radii using $m = \frac{4\pi}{3}\rho a^3$, which results in

$$\frac{4\pi}{3}\rho a_p^3 = \left(\frac{4\pi\rho}{3}\right)^2 \frac{c_f}{2-\frac{\alpha_f}{3}} \left(a_{f,\max}^{6-\alpha_f} - a_{f,\min}^{6-\alpha_f}\right). \tag{15}$$

This simplifies to

$$a_p^3 = \frac{4\pi\rho c_f}{6-\alpha_f} \left(a_{f,\max}^{6-\alpha_f} - a_{f,\min}^{6-\alpha_f}\right). \tag{16}$$

This is rearranged to solve for c_f as

$$c_f = \frac{6-\alpha_f}{4\pi\rho}\frac{a_p^3}{a_{f,\max}^{6-\alpha_f} - a_{f,\min}^{6-\alpha_f}}. \tag{17}$$

From Eq. (17), we can see that the c_f coefficient will depend on the impacting particle's radius a_p, particle's density ρ, proportionality constant $c_{\max}$ (through the dependence on $a_{f,\max}$), minimum fragment size $a_{f,\min}$, and scaling exponent α_f.

The total damage area incurred by the distribution of fragments is estimated by characterizing each individual puncture according to Eq. (7). The total area of all holes upon the exit surface is then expressed as

$$A_{\text{exit}} = \frac{\pi}{\cos\theta}\int_{m_{f,\min}}^{m_{f,\max}} n_f \kappa^2 a_f^2 \mathrm{d}m_f. \tag{18}$$

For simplicity, we assume that all fragments retain the same angle of incidence θ as the original impactor, and thus the cosine term is treated as constant in this analysis. Since the κ term is ultimately dependent on a_f, and therefore m_f, it is kept in the integral and will vary with fragment size according to the implicit dependencies within Eq. (1). Equation (18) is simple to compute numerically.

We embarked on this formulation to ultimately determine the total damage that a single micrometeoroid will cause to both sides of the lenticular, which we call A_{impact}. To estimate the total damage area in the absence of a micrometeoroid shield, we define A_{impact} as

$$A_{\text{impact}} = A_{\text{ent}} + A_{\text{exit}}, \tag{19}$$

where A_{ent} and A_{exit} are defined by Eqs. (7) and (18). It should be noted that our model assumes that the membrane material is vaporized on impact and that penetrations made on later layers are the result of the repeated fragmentation of the original impactor. This assumption is made as it is a simplification and a conservative assumption in determining the total damaged area. This assumption can be relaxed after a future test campaign with a sufficient number of shots to produce a satisfactory empirical estimate of the vaporized mass.

In Sec. 5, we will determine the gas lost through these punctures over time. The cumulative hole area, A_H, in the primary reflector is estimated as

$$A_H(t) = A_{\text{seams}} + A_R t\int_{m_{p,\min}}^{m_{p,\max}} \Phi(m_p) A_{\text{impact}} \mathrm{d}m_p, \tag{20}$$

where A_{seams} is the initial hole area due to construction of the seams, A_R is the surface area of the primary reflector, t is time, $\Phi(m_p)$ represents the micrometeoroid flux as a function of projectile mass m_p, and A_{impact} describes the hole area caused under impact conditions for the micrometeoroid's radius a_p [see Eqs. (1) and (19) for all inherent dependencies]. The $\Phi(m_p)$ term is a property of the local space environment, where the bounds $m_{p,\min}$ and $m_{p,\max}$ represent the minimum and maximum incoming micrometeoroid sizes, respectively.

2.3 *Micrometeoroid Punctures after N Shattering Events*

In Sec. 4, we discuss the possible mitigation of micrometeoroid holes through the use of a micrometeoroid shield, which consists of multiple layers of Kapton that act as a bumper for the lenticular. The total fragment mass on each consecutive interface should decrease for two reasons: vaporization and the inability of the smallest fragments to reach the ballistic limit. The goal is to fragment the micrometeoroid sufficiently so that only a few fragments remain above the ballistic limit when they arrive at the lenticular structure at the center. This will decrease the hole area with time [$A_H(t)$ in Eq. (20)] and allow the inflatant to be conserved. Because the fraction of mass that vaporizes is difficult to quantify with experiments, this paper will focus on the mass loss due to the ballistic limit.

We set up the formulation needed to propagate the fragmentation for consecutive membrane layers to determine the damage incurred on each interface. We can think of repeated fragmentation as a fractal process—each fragment can be thought of as the original impactor described in Sec. 2.2, and Eqs. (9), (10), and (17) can be evaluated in the same manner as in Sec. 2.2 to determine the secondary fragmentation of each incoming fragment.

We assume that the fragments, similar to the original projectile, further fragment according to the power law distribution in Eq. (9), with each fragment having a maximum secondary fragment size of

$$a_{f,\max,s} = c_{\max} a_f, \tag{21}$$

where the s subscript represents a secondary fragment. This means that the largest fragment out of all secondary fragments after the N'th shatter is calculated as

$$a_{f,\max,N} = c_{\max}^{N} a_p. \tag{22}$$

We again assume the fragments shatter as spheres, allowing us to define the maximum fragment mass as $m_{f,\max,N} = \frac{4\pi}{3}\rho a_{f,\max,N}^3$. For simplicity, we assume that all subsequent fragmentations maintain the same $a_{f,\min}$ as the original impactor. We also assume that fragments will not fragment further once they reach a size of $a_{f,\min}$. The number distribution of fragments at size m_f after the N'th shattering event, $n_{f,N}$, is then calculated as

$$n_{f,N}(m_f)dm_f = \sum_{i=m_{f,\min}}^{m_{f,\max,N-1}} q_i n_{i,s}, \tag{23}$$

where q is the number of incoming fragments at size i from the previous shattering, expressed as

$$q_i = n_{f,N-1}(i)dm_f, \tag{24}$$

and $n_{i,s}$ represents the number of secondary fragments of size m_f produced by the shattering of the impacting fragment of size i, which is written as

$$n_{i,s}(m_f)dm_f = c_{i,s}\left(\frac{3m_f}{4\pi\rho}\right)^{-\frac{\alpha_f}{3}} dm_f. \tag{25}$$

The scaling term $c_{i,s}$ needs to be re-calculated for each incoming fragment size i being evaluated as discussed in Sec. 2.2 (here, each impacting fragment m_i is now treated as m_p). The number distribution for $n_{f,N}$ is bounded from $m_{f,\min}$ to $m_{f,\max,N}$, as defined earlier. This fragmentation process repeats until all fragments reach a size of $a_{f,\min}$ and the particles cannot shatter any further. Although Eq. (23) appears cumbersome, it is relatively easy to implement numerically.

The total damage area incurred on the membrane after the N'th shatter is thus

$$A_N = \frac{\pi}{\cos\theta}\int_{m_{f,\min}}^{m_{f,\max,N}} n_{f,N}\kappa^2 a_f^2 \mathrm{d}m_f. \tag{26}$$

We again remind the reader that κ is not a constant but varies as a function of the micrometeoroid properties, film properties, and impacting velocities.

3 Laboratory Analysis of High Velocity Impacts on Membranes

In this section, we use hypervelocity impact tests on Kapton membranes to empirically define the parameter values for the micrometeoroid fragmentation from Sec. 2.

Table 1 Experimental design for each shot performed.

Test #	Projectile material	Projectile diameter (μm)	Calculated projectile mass (g)	Impact angle (deg)	Velocity (km/s)	Stand-off distance (m)
1	Ruby	200	1.65×10^{-5}	0	7.09	0.33
2	Ruby	200	1.65×10^{-5}	0	7.05	0.66
3	Ruby	200	1.65×10^{-5}	0	7.18	1.00
4	Ruby	200	1.65×10^{-5}	50	7.18	0.33
5	Ruby	200	1.65×10^{-5}	50	6.9	1.00
6	Ruby	200	1.65×10^{-5}	0	4.93	0.33
7	Ruby	200	1.65×10^{-5}	0	4.17	0.33

3.1 *Experimental Design and Damage Area Observed*

The purpose of these experiments is to aid us in the characterization of hole area damage for the micrometeroid environment of concern, as well as to provide data to support and validate our theoretical model, in particular, for the characterization of the impact of a micrometeoroid through an initial wall, the subsequent break-up and debris cloud, and finally the break-up and cloud's impact upon the second wall.

All testing was performed at NASA WSTF. A shot matrix was developed with the purpose of characterizing the hole area as a function of the projectile's velocity, the two target surface's stand-off distance, and the impact angle. The test shot matrix is given in Table 1. Due to testing restraints, we were not able to test a sampling of projectile diameters or masses.

To accurately model the micrometeoroid environment, a 200-μm diameter aluminum oxide (Al_2O_3, ruby, density 3.95 g/cm^3) projectile, decided upon by a conference of subject matter experts at WSTF, is used. Prior to each test, the projectile mass was measured using a Mettler Toledo XP56 Delta Range balance ($\pm$0.001 mg), and the projectile diameter was measured using a Geller microanalytical laboratory micro-ruler ($\pm$0.01 mm).

The tests use kapton samples manufactured at Northrop Grumman Space Park. This is representative of the current choice of the membrane for the OASIS mission concept with a design that is based on an inflatable lenticular. The target samples are kapton sheets of 0.5 mil (12.7 μm) thickness, cut to $\sim$12 in. square. The film samples are secured in frames as pictured in Fig. 3, setting them to the appropriate incline angle and stand-off distance for a specified test shot

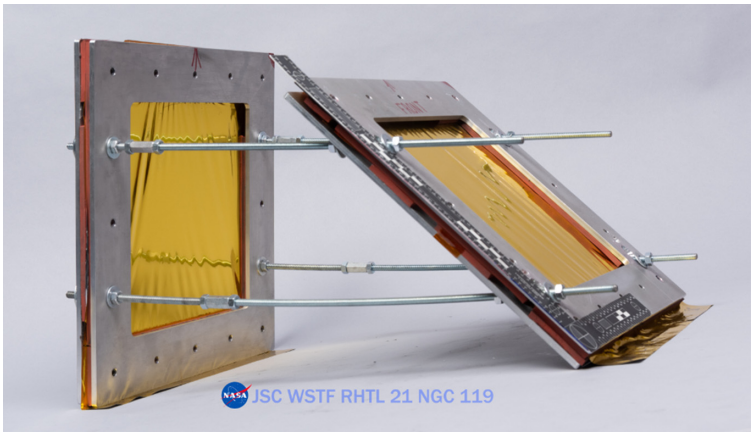

Fig. 3 Test article setup. The first (right) membrane is set to the specified impact angle, and the second (left) membrane surface is always set to a zero incidence angle. The stand-off distance between the membranes is varied for each test shot.

(see Table 1). The samples were secured in a manner such that they each experienced a tensile load of 1000 pounds per square inch (ksi, a unit of stress). This load is reflective of the pressure that would be experienced by the membrane when fully inflated. The ~1 ksi stress level was achieved by attaching a small weight to the bottom part of the target membrane. The first membrane is set to a specified incidence angle given in Table 1, and the second membrane remained at an incidence angle of zero for all test shots (see Fig. 3).

Seven impact tests were performed for a 200-μm diameter ruby projectile upon the two consecutively placed 0.5 mil (12.7 μm) thick Kapton membranes. Images of the membranes were used to determine the damage area on each surface. Impact holes were identified by eye, and the perimeters of the holes were defined. The damage area in pixels^2 was calculated and subsequently converted to mm^2 using a scale bar on the image. Due to the large number of holes on each second membrane after fragmentation, a high density and low density damage region is defined. These regions are then divided into quadrants. A quadrant is selected to manually identify all impact holes, and the cumulative area is multiplied by four to calculate the total damage in that region. Table 2 gives the total damage area observed on each membrane.

To further illuminate the image analysis method described above, let us look at the case of the sixth shot (Table 1). Figure 4 shows the damage to the entrance membrane. The particle creates a well-defined, circular hole that can be directly used to determine the κ value for the particle's size and velocity (see Sec. 3.3). The other test shots also displayed circular impacts on the first membrane, with the exception of shots 4 and 5, which impacted at an incidence angle of 50 deg. The wounds from these impacts were elliptical in shape, consistent with Eq. (7). The total damage area to the entrance membrane, $A_{\mathrm{ent,obs}}$, observed on each test shot is given in Table 2.

Figure 5 shows the damage incurred on the exit membrane on shot 6. It is clear that the test particle has completely disrupted into many fragments, creating holes of various sizes.

Table 2 Total damage observed on each membrane.

Test #	Total damage to first membrane (μm^2)	Total damage to second membrane (μm^2)
1	5.88×10^4	2.53×10^6
2	5.89×10^4	2.44×10^6
3	6.29×10^4	1.80×10^6
4	9.83×10^4	3.93×10^6
5	8.88×10^4	1.47×10^6
6	6.05×10^4	1.28×10^6
7	5.06×10^4	1.07×10^6

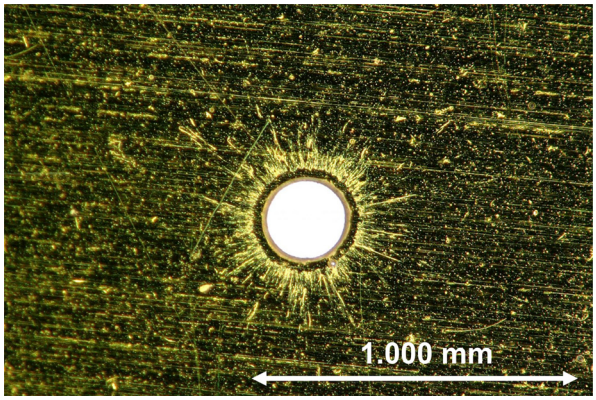

Fig. 4 Damage to the first membrane of shot 6. A single, circular hole is observed.

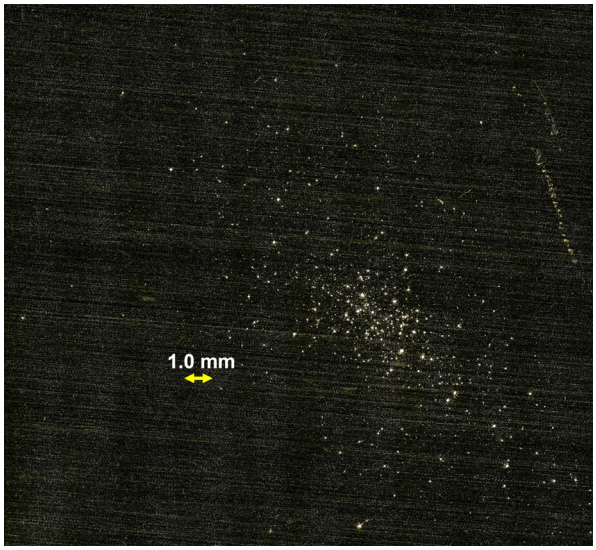

Fig. 5 Damage to the second layer of shot 6. The impactor completely disrupts after impact with the first layer, resulting in fragments that create many holes on the second membrane. A high density damage region is observed in the center, surrounded by a diffuse region of damage.

These fragments create a high density region of damage in the center, with more diffuse damage occurring further on the outer edges.

The impact hole identification and measurements were performed manually by the authors as resources to automatically and accurately identify impacts were unavailable. The manual method of dividing the image into non-adjacent regions and then scaling the count to estimate the total number of holes was inspired by author Arenberg's experience using a hemocytometer to count bacteria in a high school biology class. The distributions of the holes in both the high- and low-density regions are observed to be fairly uniform and align with physical and statistical intuition. Due to these observations and time limitations, a single quadrant, rather than the whole four quadrants of these low- and high-density regions, was measured. Later it was confirmed that statistics of the counts also align with these observations. This is elaborated on in Sec. 3.2. Based on the fragment sizes inferred, the authors do not believe a large error was introduced using the quadrant method.

The high density region of damage is identified in Fig. 6. The lower right quadrant is selected, and every hole identified in that quadrant is measured, with measurements represented in the

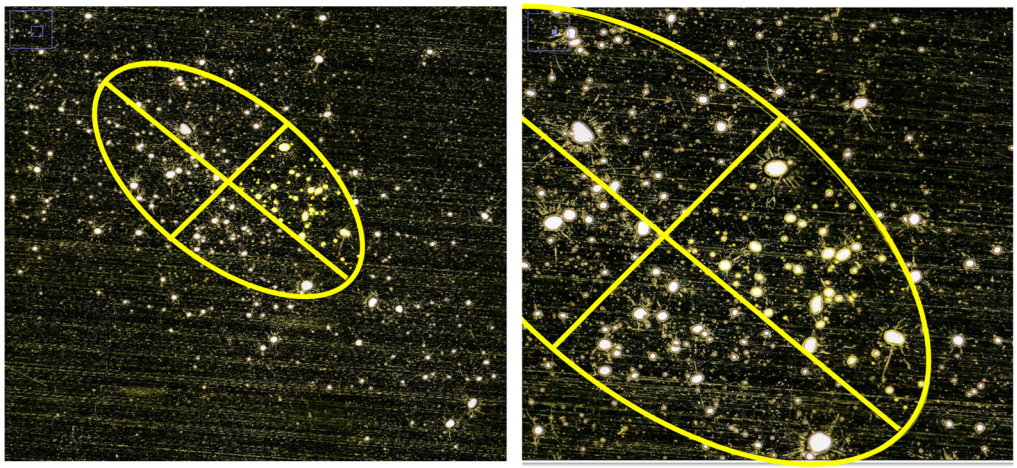

Fig. 6 High density region on the second membrane of shot 6. (a) The high density region is defined and split into quadrants. A quadrant is selected (lower right) to manually measure each hole. (b) Close up of quadrant measurement.

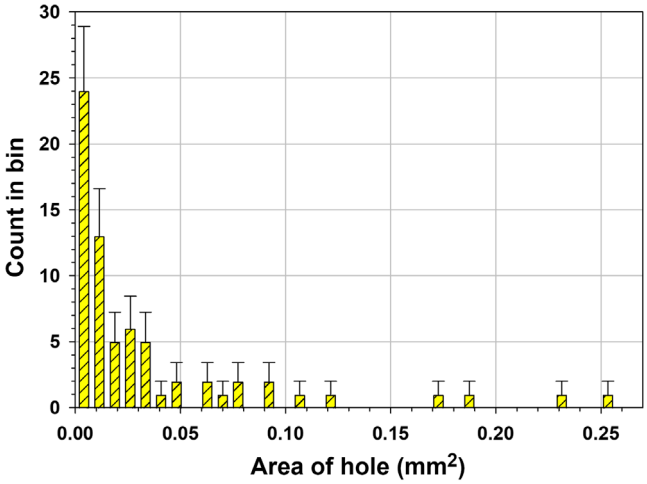

Fig. 7 Depiction of the size distribution of damage holes upon the back layer of shot 6 for the high density region, with square root of count error bars. As can be seen, the damage area follows a power law distribution.

ImageJ software by a yellow circle. All measurements were exported to an excel document and then summed to get the full damage area of the quadrant. The quadrant area is multiplied by four to achieve the high density region's total damage area, A_{High}. The distribution of holes in this region is seen to follow a power law distribution as expected (Fig. 7).

The low density region of damage is identified in Fig. 8. The upper right quadrant is selected, and every hole identified in that quadrant is measured, with measurements represented in the ImageJ software by a yellow circle. The distribution of holes in this region is seen to follow a power law distribution as well (Fig. 9). Compared with the high density region, which contains a higher percentage of larger-sized holes, the low density region has a higher percentage of smaller-sized holes.

Because the high density region is contained within the low density region, we have to subtract the contribution of the high density region from the low density quadrant counts to avoid double counting. The total areal damage in the low density region, A_{Low}, is then calculated as

$$A_{\mathrm{Low}} = 4(A_{q,\mathrm{Low}} - \gamma A_{q,\mathrm{High}}), \tag{27}$$

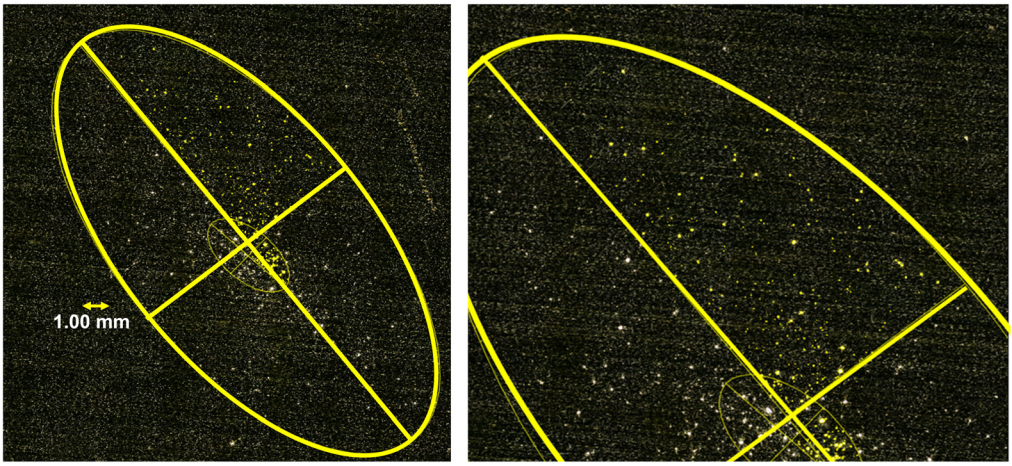

Fig. 8 Low density region on the second membrane of shot 6. (a) The low density region is defined and split into quadrants. A quadrant is selected (upper right) to manually measure each hole. (b) Close up of quadrant measurement.

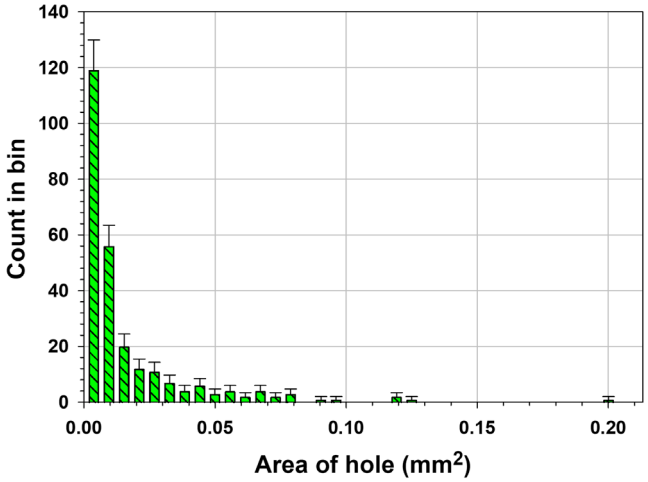

Fig. 9 The figure above depicts the size distribution of damage holes upon the back layer of shot 6 for the low density region. As can be seen, the damage area follows a power law distribution.

where $A_{q,\mathrm{Low}}$ and $A_{q,\mathrm{High}}$ are the total damage measured in the quadrants of the low density and high density regions, respectively, and γ represents the fractional area of the low density region occupied by the high density region. This quantity is multiplied by four to get the total damage over all four low density quadrants. The total damage to the exit membrane is then calculated by $A_{\mathrm{exit,obs}} = A_{\mathrm{High}} + A_{\mathrm{Low}}$, given in Table 2.

All seven shots exhibit a similar behavior for fragmentation and follow a power law distribution for hole sizes. Table 2 gives the total damage area observed on each membrane. Some variation in the damage distribution was observed with stand-off distance (i.e., high density and low density regions are less well defined for greater distances). However, it was difficult to determine the role of the stand-off distance in the total damage incurred because the velocity on each shot also changed. More data is needed to properly characterize this effect.

3.2 *Error Analysis on Counting*

This section focuses on the error analysis of the damaged area from the hypervelocity test series that were recently carried out.

3.2.1 *Entrance surface wound*

The experimentally derived value of κ is the ratio of the diameter of the hole in the entrance membrane, D_h, to the diameter of the penetrator, d_p.

The variance in κ is found by applying the law of error propagation to Eq. (4), which is written as

$$\sigma_\kappa^2 = \left(\frac{\partial \kappa}{\partial D_h}\right)^2 \sigma_{D_h}^2 + \left(\frac{\partial \kappa}{\partial d_p}\right)^2 \sigma_{d_p}^2. \tag{28}$$

Substitution of the partial derivatives in Eq. (28) gives

$$\sigma_\kappa^2 = \left(\frac{1}{d_p^2}\right)\sigma_{D_h}^2 + \left(\frac{D_h^2}{d_p^4}\right)\sigma_{d_p}^2. \tag{29}$$

Because the variances of D_h and d_p can be expressed as a fraction of their values by the ratios g and h, respectively, we write

$$\sigma_\kappa^2 = \left(\frac{1}{d_p^2}\right)(D_h^2 g^2) + \left(\frac{D_h^2}{d_p^4}\right)(d_p^2 h^2). \tag{30}$$

The value of g is derived from the measurements of the diameter of the entrance wound. On the basis of repeated measurements of the entrance wounds on many different diameters, we estimate that the precision on the measurement of D_h is on the order of $0.03D_h$ or 3%. The value of h is a fractional error in d_p and is the root-sum-square of the effects of non-sphericity of 0.32% and average diameter error of 0.64%. These values combined give h as 0.71%. So the estimated fractional error in κ is ~3.1%

3.2.2 *Exit surface wound*

In this section, we discuss our estimation of the uncertainty in determining the penetration area of the exit surface. This area is made up of many small holes counted and sorted into size bins as shown in Fig. 7 and referenced to the high or low density region. We write the total area of penetration of the membranes, $A_{\text{exit,obs}}$ as

$$A_{\text{exit,obs}} = 4\left[\left(\sum_{i=1}^{w} L_i \pi r_i^2\right) + (1-\gamma)\left(\sum_{i=1}^{w} H_i \pi r_i^2\right)\right], \tag{31}$$

where the area of penetration in each quadrant is replaced by summations over a fixed number of bins and the correction term γ to avoid double counting. To formulate the variance in $A_{\text{exit,obs}}$, the law of error propagation is applied to Eq. (31), giving

$$\sigma_{A_{\text{exit,obs}}}^2 = \sum_{i=1}^{w}\left(\frac{\partial A_{\text{exit,obs}}}{\partial L_i}\right)^2 \sigma_{L_i}^2 + \sum_{i=1}^{w}\left(\frac{\partial A_{\text{exit,obs}}}{\partial H_i}\right)^2 \sigma_{H_i}^2 + \left(\frac{\partial A_{\text{exit,obs}}}{\partial \gamma}\right)^2 \sigma_\gamma^2. \tag{32}$$

Evaluation of the partial derivatives in Eq. (32) gives

$$\sigma_{A_{\text{exit,obs}}}^2 = \sum_{i=1}^{w}(4\pi r_i)^2 \sigma_{L_i}^2 + \sum_{i=1}^{w}((1-\gamma)4\pi r_i)^2 \sigma_{H_i}^2 + (4A_{q,H})^2 \sigma_\gamma^2. \tag{33}$$

Reorganization of Eq. (33) gives

$$\sigma_{A_{\text{exit,obs}}}^2 = (4A_{q,H})^2 \sigma_\gamma^2 + 4\pi \sum_{i=1}^{w} r_i^2(\sigma_{L_i}^2 + (1-\gamma)\sigma_{H_i}^2). \tag{34}$$

The leftmost term in Eq. (34), is due to variance in γ and the terms under the summation signs are the expected variances in the counts of the various bins in the high and low regions. An experiment was performed to determine the variance in γ. The analyst divided up the area from a pristine image and then measured the γ for each trial. The standard deviation in γ was $\sim 0.1\gamma$ and substituted into Eq. (34). The variances in the counts in the bins L_i and H_i are determined by Poisson statistics, and the variance is replaced by the mean and shown in Eq. (35)

$$\sigma_{A_{\text{ent,obs}}}^2 = 0.01(4A_{q,H})^2 + 4\pi \sum_{i=1}^{w} r_i^2(L_i + (1-\gamma)H_i). \tag{35}$$

Because most of the area of the exit wound is found in bins with a large number of counts, the fractional variance is significantly <0.01, so the first term is dominant, and the standard uncertainty in the exit area is ~10%.

3.3 *Observed Impacts on the First Membrane and Determination of Parameter Beta*

In Sec. 2.1, we reviewed the theoretical formulation for the hole diameter size as a function of the projectile properties, film properties, and impacting velocity [Eq. (1)]. For this formula to be useful for extrapolating κ to higher velocities, we need to determine the values for β_1 and β_2 in Eq. (3) for Kapton. In our experiments, all variables in Eq. (1) are held constant except for the velocity, allowing us to determine the velocity dependence of β.

The hole diameter sizes measured on the entrance membranes give a corresponding ratio of $D_h/f \approx 20$. In this regime, Eq. (1) is approximated as

$$d_p' \approx D_h'(1 - \exp(-D_h'/\beta)). \tag{36}$$

This is written in terms of κ as

$$\frac{1}{\kappa} = 1 - \exp(-D_h'/\beta). \tag{37}$$

Solving for parameter β then gives

$$\beta = \frac{-D_h'}{\ln\left(1 - \frac{1}{\kappa}\right)}. \tag{38}$$

Because the first membrane displays damage from when the projectile was still intact, calculating κ for each shot is straightforward using Eq. (4). The shots display a modest change in κ, ranging from 1.27 to 1.42 over this small velocity range, with an average value of $\kappa = 1.37$. The calculated κ and the observed hole size D_h are plugged into Eq. (38) to determine the corresponding β parameter for each shot. Figure 10 shows the variation in β with velocity. The magenta dashed line in Fig. 10 is the line of best fit for the data points. We use this best fit line to describe how β varies with velocity and find $\beta_1 = 13.3$ and $\beta_2 = 0.55$ in Eq. (3). Thus, we define β for Kapton as $\beta = 13.3 + 0.55$ V, where the velocity is in units of km/s. We note here that this is a small sample size and more hypervelocity tests are needed to accurately determine β_1 and β_2.

Using the above definition for β, we produce κ curves for the experiment at different velocities using Eqs. (1) and (4), as shown in Fig. 11. We use values representative of Kapton and ruby, with inputs set to $f = 12.7$ μm, $\sigma_t = 8.79 \times 10^7$ Pa, $\rho_t = 1380$ kg/m^3, and $\rho_p = 3950$ kg/m^3. These curves clearly demonstrate that impactors that are large relative to the membrane thickness exhibit minimal increases in κ with an increase in velocity. The figure

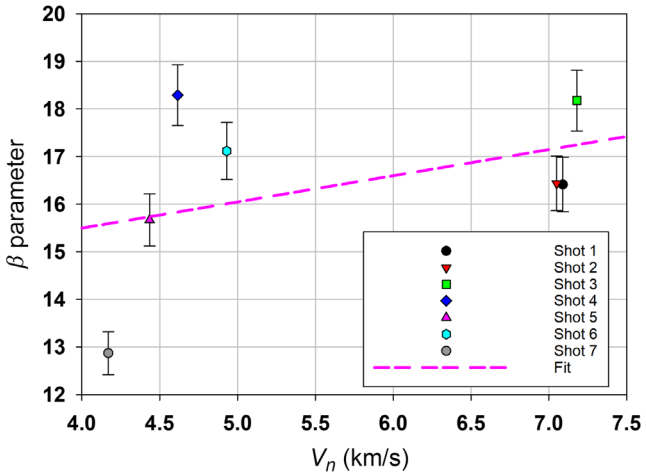

Fig. 10 Variation in β parameter with velocity. The dashed line is the line of best fit and is used to calculate the values for β_1 and β_2.

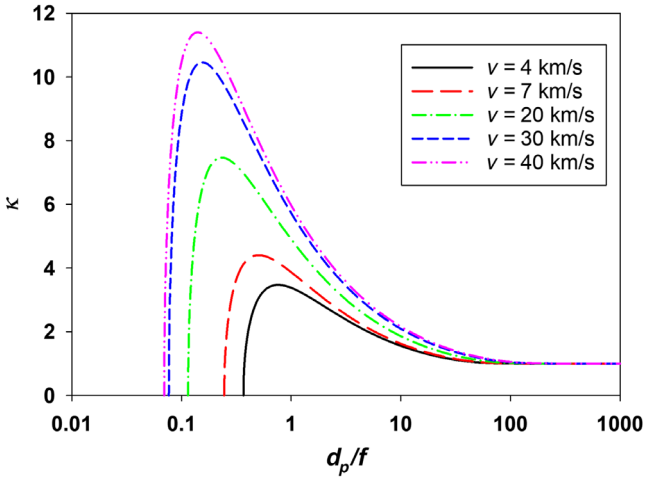

Fig. 11 Variation of κ for a ruby impactor on a 0.5 mil Kapton film. κ varies with both the ratio of the projectile diameter (d_p) to the film thickness (f) and the velocity of the impactor.

also illustrates how κ rapidly increases as the projectile size becomes small relative to the membrane thickness, until it reaches the ballistic limit ($\kappa = 0$). Our experimental setup corresponds to an initial ratio of $d_p/f = 15.75$ and range in velocity from 4 to 7 km/s. However, after the micrometeoroid shatters, we expect its fragment distribution to span the full range of ratios less than this value, which correspond to maximum κ values of 3.5 to 4.5 over this velocity range. If future tests are performed at speeds more representative of micrometeoroids (~35 km/s, Thorpe et al.,[7]), we expect the maximum κ values for those experiments to be closer to 10, as indicated by the blue line in Fig. 11.

3.4 *Observed Impacts on the Second Membrane and Implications for Fragmentation*

One of the goals of this paper is to empirically determine what the parameter values should be for micrometeoroid fragmentation. This requires examining the fragment distribution from our experiments to extract α_f and $c_{\max}$ (which then determines $a_{f,\max}$), which dictate this distribution. Although $a_{f,\min}$ also influences the overall distribution, it does not affect the distribution as much as the other two parameters because that limit controls a small fraction of the total mass. Values acquired for α_f and $c_{\max}$ can then be used to feed into a predictive model for the fragmentation.

The experiments performed directly measure the damage area caused by impacting fragments, not the fragment sizes themselves. Therefore, the number distribution of the fragments must be inferred. We utilize Eq. (1) to estimate the impacting fragment sizes that produced the observed holes on the second membranes. Because we do not know the individual velocities of each fragment, we make the simplifying assumption that all fragments will have impacting speeds equal to that of the original impactor. The d_p/f curves (similar to Fig. 2) are produced for each shot's corresponding impact velocity to allow us to map the observed hole diameter D_h to a corresponding fragment diameter d_f. It is worth noting that, as we learned from Fig. 11, lower impact velocities will shift the kappa curve downward; therefore, if the fragment velocities are actually less than the original impactor velocity that we used to map the fragment sizes, we would expect the largest errors in our inferred fragment sizes for the smallest fragment bins observed where the curves deviate the most (left side of the curve in Fig. 11).

A fragment array is created to bin fragment diameters ranging from 2 μm (just below the ballistic limit for Kapton at these speeds) to 200 μm (the original particle diameter) with a bin spacing of 4 μm. To arrive at an inferred number distribution, we calculate the D_h/f ratio for each hole observed to determine the corresponding fragment diameter d_f and add a number count to the bin encompassing the matched fragment size. A check is performed to ensure that

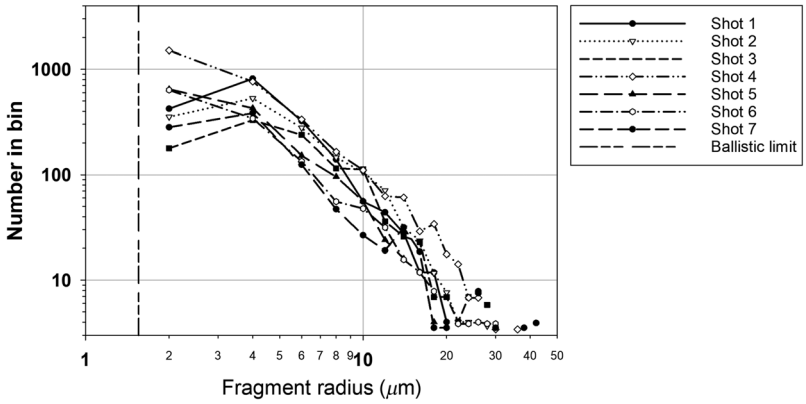

Fig. 12 Fragment size is inferred from each damage hole observed. The fragments are then binned and counted. The dashed line indicates the ballistic limit for an impacting velocity of 7 km/s. Midpoints of the bins are used to plot the data.

all observed holes are assigned to a bin. Because the hole measurements are counted for a single quadrant, the number counts are multiplied by four to estimate the total number of fragments penetrating the membrane. We use a correction similar to Eq. (27) to subtract the high density region contribution to the low density counts to avoid double counting holes.

Figure 12 shows the resulting number distributions from each impact test as a function of fragment radius. All shots exhibit similar behavior for the fragmentation and follow a power law distribution as expected. The dashed line in Fig. 12 is the ballistic limit calculated using Eq. (8) for a reference velocity of 7 km/s. It is worth noting that there is a sharp drop-off in counts for the smallest fragment bins. This could be due to the fragments having a lower impact velocity than the original impactor (and thus $d_{p,\mathrm{bal}}$ would be larger), particles not penetrating the membrane efficiently, difficulty observing the smallest holes, or all of the above.

As a sanity check to make sure that our results make physical sense, we sum over all fragment masses for each inferred number distribution and compare this value with the original impactor mass. This sum should always be less than or equal to the original impactor mass. We approximate the fragments as spheres and use the relation $m = \frac{4\pi}{3}\rho a_f^3$ to calculate the mass of each fragment. Figure 13 shows this sanity check for each test shot. Almost all shots are consistent with the conservation of mass and have similar values for $(\sum m_f)/M_p$ with a median value of ~0.8. Shots 4 and 5 appear to be anomalies, with mass fractions of about 1.6 and 0.31,

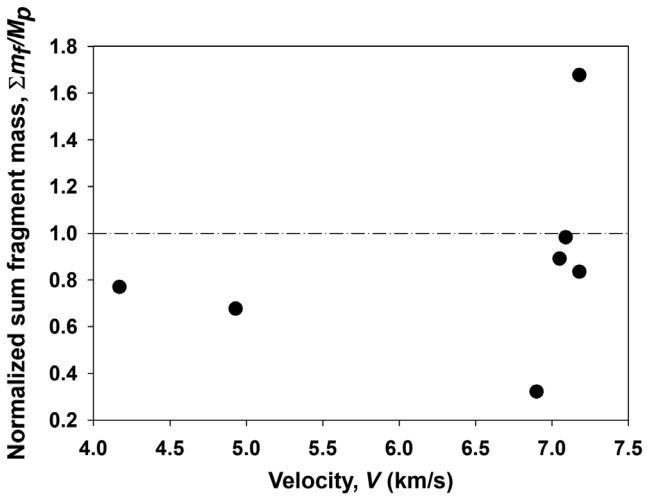

Fig. 13 All inferred fragment masses from Fig. 12 are summed to determine the total fragment mass. The ratio of the total fragment mass to the original projectile mass (M_p) is shown. These values should always be less than or equal to the projectile mass.

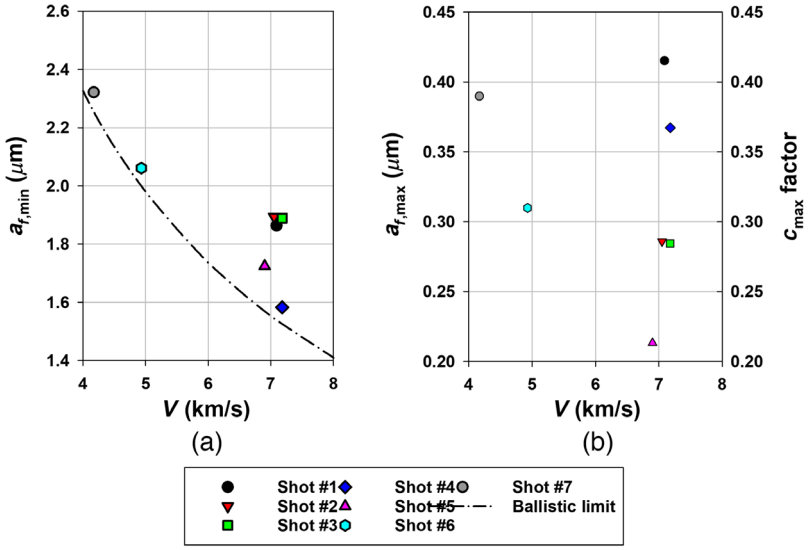

Fig. 14 (a) The minimum fragment size observed on each shot is near the ballistic limit (dashed line). (b) Maximum fragment size observed on each shot (lefthand *y*-axis) and the scaling factor derived based on the maximum fragment size (righthand *y*-axis).

respectively. It is worth noting that these are the two experiments in which an incidence angle on the first membrane was imposed, which may affect the inferred fragment size. There are also other possible explanations for this error. The first is that we approximate all projectile fragments as spheres. The shapes of the shards after every test completion were not examined, so it is hard to say how much the fragments deviate from a spherical shape. Future tests would be needed to determine their elongation. Other error contributions could be due to the assumptions in κ and the count extrapolation from the quadrant method. Assuming shots 1, 2, 3, 6, and 7 are good representations of the true fragment mass, Fig. 13 suggests that about 17% of the mass is lost after the first membrane due to the inability of the smallest fragments to penetrate the second membrane at these speeds.

In addition to the number distribution, we also want to determine the bounding limits of the fragmentation. The smallest and largest holes observed for each shot are identified, and a corresponding fragment size is calculated. Figure 14(a) shows that the smallest holes observed correspond to fragment sizes that are at or just above the ballistic limit (dashed line). This implies that the true value for $a_{f,\min}$ of the fragment distribution is likely smaller than this, but it cannot be observed because these fragments are not able to penetrate the membrane. Figure 14(b) shows that the test shots exhibit similar sizes for their observed $a_{f,\max}$. Because the particle size is held constant throughout our experiments, this also gives rise to consistency in the calculated $c_{\max}$ value. We find an average value of $c_{\max} = 0.32$, with the overall range encompassing the $c_{\max} = 0.22$ (Jones et al.,[9]) and $c_{\max} = 0.27$ (Hirashita and Kobayashi,[10]) values assumed in the literature.

To establish a model that is representative of particle fragmentation incident on a polyimide film, we need to determine which combination of α_f and $c_{\max}$ best replicates the observed fragmentation. The fragmentation is modeled using Eqs. (9), (10), and (17) to ensure conservation of mass. We use as inputs the original impactor mass, radius, and ρ as defined by the experimental setup (see Table 1). We set $a_{f,\min} = 1$ μm, just below the ballistic limit, because the true value could not be determined. The α_f and $c_{\max}$ parameters are varied to determine which combination produces the minimum residuals. The α_f parameter is varied from 3 to 5.5 with 0.1 increments, and $c_{\max}$ is varied from 0.20 to 0.40 with 0.01 increments. Because the smallest and largest fragment bins have issues with their counting statistics, we limit the fit to fragments with radii between 3 and 18 μm. We find that the data is best fit by a fragmentation model with parameters $\alpha_f = 4$, $c_{\max} = 0.24$, and $a_{\min} = 1$ μm. Figure 15 shows how the number distribution estimated from this model compares with the number distributions inferred from the observed impacts.

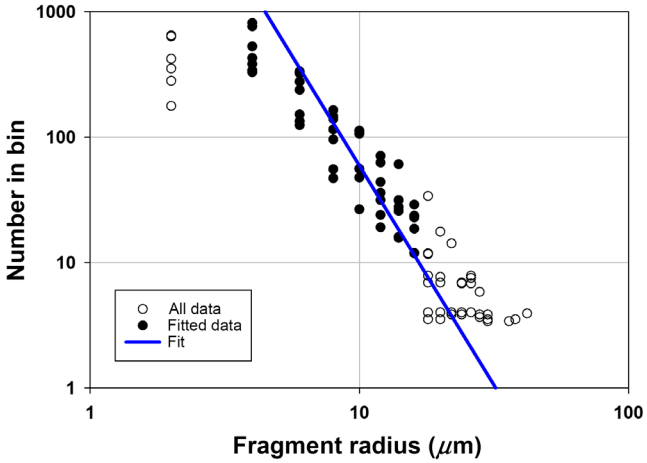

Fig. 15 Observed number distributions from the hypervelocity impact tests are best described by a fragmentation model with $\alpha_f = 4$ and $c_{\max} = 0.24$.

Our estimate for α_f is slightly larger than the values used for interstellar grain fragmentation, which typically assumes an α_f between 3.3 and 3.5.[8,9,10] The $c_{\max}$ retrieved is intermediate between the literature values of 0.22 (assumed by Jones et al.,[9]) and 0.27 (assumed by Hirashita and Kobayashi,[10]).

As a sanity check, we use our empirical model to predict impact holes on the second membrane and compare with our observed results. We set $\alpha_f = 4$, $c_{\max} = 0.24$, and $a_{f,\min} = 1$ μm to recreate a number distribution for the shattering fragments impacting the second membrane. We use the velocities given in Table 1 to determine the appropriate κ for each fragment (we assume that the fragments have the same speed as the original impactor) and use Eq. (18) to predict what the corresponding total damage to the second membrane should be. Figure 16 shows how well our model replicates the observed values from our experiments. For the most part, our model replicates the observed damage fairly well. The outlier data point near (0.017, 0.039) is shot four, which we acknowledged earlier as an an anomalous data point, perhaps due to the effects of the inclined first membrane that are not captured by our model.

3.5 *Predictions for Future Tests with Multiple Membranes*

One option to conserve the inflatant and extend the mission lifetime is to construct a robust design. A natural reaction would be to consider thicker membranes. This is likely not the

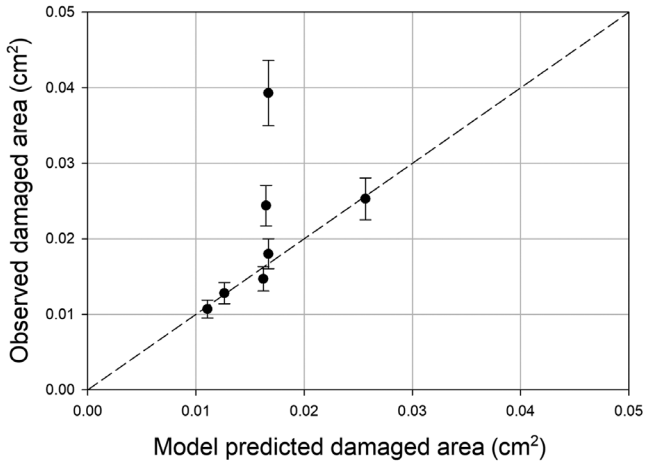

Fig. 16 Comparisons of the total damage to the second membrane predicted by our empirical model and that observed in our experiments. The dashed line represents the $y = x$ line.

solution: to achieve the relevant stress in the film needed to make a good reflector, the pressure would need to be increased for a thicker membrane. In Sec. 5, we show that the gas loss through holes [Eq. (44)] is proportional to the product of the hole area and the pressure. Thus, the cumulative hole area would have to fall off faster than linearly to extend the lifetime. Figure 11 displays that the film thickness would have to be significantly increased for the κ (which controls the overall damage) to be significantly reduced for the smallest impacting particles, which enact the most damage relative to their size. This will become clearer in Sec. 4, where we consider different membrane thicknesses.

An alternative to thicker membranes is the option of additional membrane layers to shield the central structure. These layers are added to cause successive fragmentation and reduce penetration of the lenticular. The effectiveness of such a shield will need to be validated with additional hypervelocity tests. In anticipation of such tests, we use the empirical model from the previous section to predict the damage that the fragments will cause on each subsequent layer. This will allow us to test our fragmentation model in future laboratory experiments. We keep the velocity constant to show the effects of increasing the particle size for clarity, and the inputs into the predictive model can be adjusted to forecast the damage for any experimental design.

To estimate the damage of a ruby projectile on N number of layers, we apply our model using $\alpha_f = 4$, $c_{\max} = 0.24$, $a_{f,\min} = 1$ μm, impacting velocity $V = 7$ km/s, impacting angle $\theta = 0$ deg, and a variable κ that is dependent on the projectile diameter to the film thickness (this is the red curve of κ for $V = 7$ km/s shown in Fig. 11). We set each layer to the same thickness of 0.5 mil (12.7 μm) and use values representative of Kapton for their composition. In this analysis, we consider a setup of four consecutive layers.

We estimate the damage for four initial projectile diameter sizes: 100 μm (2.07×10^{-6} g), 200 μm (1.65×10^{-5} g), 1000 μm (2.07×10^{-3} g), and 2000 μm (1.65×10^{-2} g); these sizes are reflective of the largest sizes of the micrometeoroid population that could penetrate the most layers [see Eq. (4) and (19)]. We utilize Eqs. (23) and (26) to calculate the expected fragmentation and corresponding damage area upon each membrane. Figure 17 shows an example for a

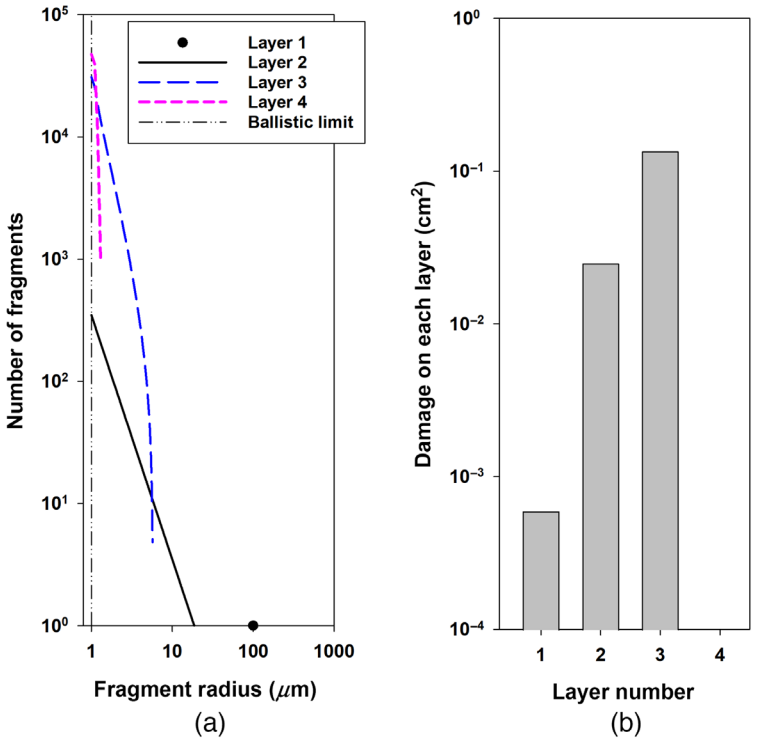

Fig. 17 Predictions for a 200-μm diameter ruby impacting four layers of 0.5 mil Kapton at 7 km/s. (a) Number distributions for fragments capable of penetrating the membrane after each subsequent shatter. The dashed line indicates the ballistic limit for the membrane. (b) Total damage predicted on each subsequent membrane layer.

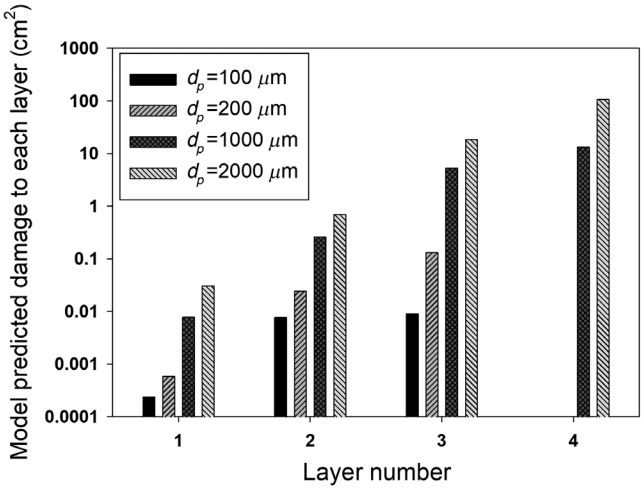

Fig. 18 Total damage area on each membrane layer (0.5 mil Kapton) is predicted for four ruby particle sizes.

200-μm incoming particle, the same as that used in our laboratory tests from Sec. 3. Figure 17(a) shows the remaining distribution of the fragments after each layer impact. The number of fragments sharply increases as the micrometeoroid is pulverized into smaller grains. However, as these fragments become smaller and smaller, they do not possess enough momentum to exceed the threshold set by the ballistic limit (dashed line in Fig. 17), resulting in mass loss after each interface. The Fig. 17(b) shows the total damage incurred by each layer. As the fragments become more numerous and smaller (larger κ), there are more punctures on each consecutive membrane, corresponding to an increase in damage that is incurred. However, there is a turning point at which enough mass is lost that the damage begins to decrease. For this example, the third layer is the most perforated, and the particles thereafter are too small to penetrate the fourth layer.

Figure 18 shows the results for damage caused by a ruby projectile with a diameter of 100, 200, 1000, or 2000 μm. The model predicts that there will be no fragments capable of penetrating the fourth membrane for initial projectile sizes of 100 and 200 μm. However, the larger particles at 1000- and 2000-μm penetrate all four layers.

It is worth noting that, in this analysis, we assume that the fragments maintain the 7 km/s speed after each interface to determine the ballistic limit and corresponding κ. Because the fragments lose energy upon each impact, the predicted damage areas are a bounding worst case scenario. In addition, we set the minimum fragment radius to be 1 μm. The actual minimum fragment radius may be smaller than this, and therefore mass could be lost at each interface more quickly than that predicted here. More experiments are needed to establish how efficiently micrometeoroid grains are removed after each obstruction.

4 Micrometeoroid Mitigation

In Sec. 5, we find that the total gas mass required to accommodate the inflated lenticular is proportional to the mission lifetime squared. This requirement is heavily dependent on the rate at which the lenticular accumulates holes in its surface due to micrometeoroid impacts. Therefore, if we can reduce the hole accumulation rate, we can extend the lifetime of the inflatant substantially. In this section, we investigate how many layers would be required to create a micrometeoroid shield capable of mitigating incoming micrometeoroids at a location near 1 AU. In addition, the same dynamics will occur for structures with multiple membranes, such as sunshields, allowing the analysis to serve multiple functions.

To assess which micrometeoroids will be the most problematic, we employ the sky-averaged micrometeoroid flux model by Grün et al.[11] to describe the micrometeoroid environment at 1 AU. This model is valid for micrometeoroid masses $10^{-18} < m_p < 1$ g and characterizes the integral micrometeoroid flux as a function of minimum threshold mass m_p as

$$\Phi(m_p) = 3.15576x10^7(F_1(m_p) + F_2(m_p) + F_3(m_p)), \tag{39}$$

where

$$F_1(m_p) = (2.2x10^3 m_p^{0.306} + 15)^{-4.38}, \tag{40}$$

$$F_2(m_p) = 1.3x10^{-9}(m_p + 10^{11}m_p^2 + 10^{27}m_p^4)^{-0.36}, \tag{41}$$

$$F_3(m_p) = 1.3x10^{-16}(m_p + 10^6 m_p^2)^{-0.85}. \tag{42}$$

Figure 19 shows the micrometeoroid flux near 1 AU. About 90% of micrometeoroids near 1 AU will impact with speeds of 35 km/s or less.[7] At a speed of 35 km/s, a large portion of the micrometeoroid flux ($m_p < 10^{-12}$, red region in Fig. 19) will not have enough momentum to penetrate a 0.5 mil Kapton membrane. Hence, a significant portion of the micrometeoroid population is mitigated due to their relative speeds alone. The remaining population presents a hazard to the inflatable lenticular. There is ~10 orders of magnitude difference in flux between particles at the ballistic limit and the maximum 1 g size considered, with a rapid drop in flux for micrometeoroids larger than 10^{-8} g.

Although in Sec. 3.5 we found that the total damage area on each successive membrane quickly scales with the original mass of the incoming micrometeoroid (Fig. 18), impacts due to large-sized micrometeoroids occur much less frequently. For example, Fig. 19 indicates that micrometeoroids greater than 10^{-5} g occur at a rate of <1 per year per m^2. Hence, there is a trade-off between size and frequency that must be considered to determine how quickly a micrometeoroid shield will incur damage.

We utilize the information gathered from our laboratory tests and apply it to the real-world space environment. The interaction is modeled for the case of micrometeoroids impacting a lenticular membrane protected by sacrificial shield layers that are all composed of Kapton sheets, each with the same thickness. The parameter values for the fragmentation obtained in Sec. 3.4 are used to extrapolate results for velocities reflective of micrometeoroids. We assume that a silicate micrometeoroid ($\rho = 2.5$ g/cm^3[11]) fragments in the same manner as that observed for the ruby test particles, with $\alpha_f = 4$, $c_{\max} = 0.24$, and $a_{f,\min} = 1$ μm. We implement the β parameter observed for Kapton in Sec. 3.3 and set $\beta_1 = 13.3$ and $\beta_2 = 0.55$.

The total damage is estimated for three cases of membrane thickness: 0.5 mil (12.7 μm), 1 mil (25.4 μm), and 2 mil (50.8 μm). Analysis is performed for an incidence angle of $\theta = 0$, a velocity reflective of micrometeoroids near 1 AU of $V = 35$ km/s,[7] and particle masses of 10^{-12} to 1 g. The lower bound of this mass limit corresponds to the ballistic limit for the

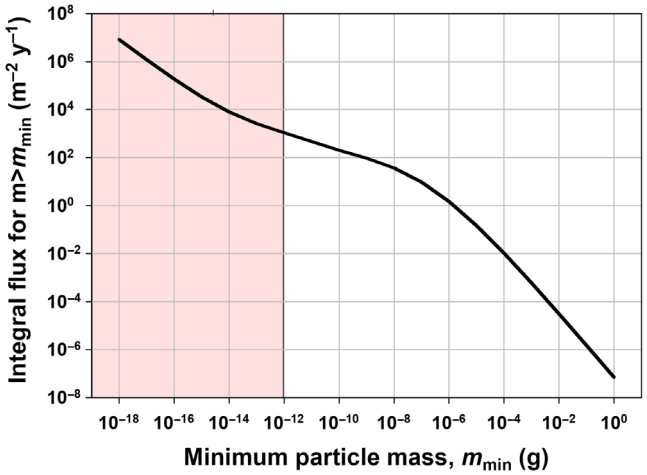

Fig. 19 Grün et al.[11] model for the micrometeoroid flux near 1 AU. Micrometeoroids less than 10^{-12} g (shaded gray region) with impact speeds of ≤35 km/s will not penetrate a 0.5 mil (or thicker) Kapton film.

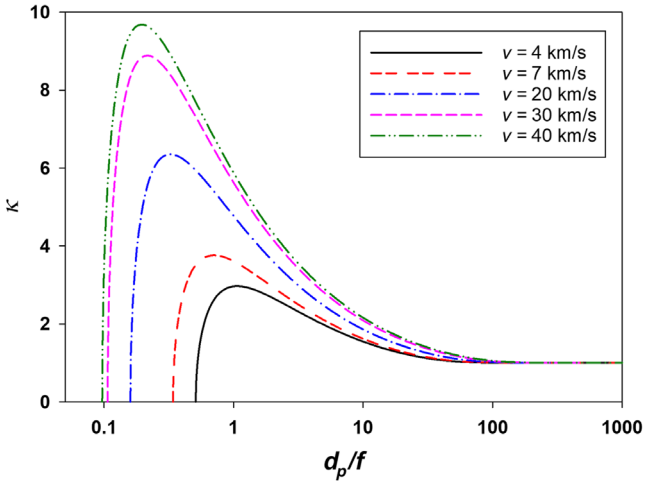

Fig. 20 Variation of κ for a silicate micrometeoroid impactor on a 0.5 mil Kapton film. κ varies with both the ratio of the projectile diameter (d_p) to the film thickness (f) and the velocity of the impactor.

0.5 mil thickness case (the other cases require a minimum mass larger than this to penetrate). We use Eqs. (1) and (4) to determine the κ values for all d_p/f ratios, as shown in Fig. 20. Fragments are assumed to maintain the same speed as the original impactor. Equation (26) is then used to determine the resulting damage on each wall. Figure 21 shows the damage area caused on successive 0.5 mil layers for an incoming micrometeoroid of mass m_p. The increasing drop-off in the damage distribution depicts the survivability of the fragments and demonstrates the minimum micrometeoroid mass needed to reach a layer N. For example, micrometeoroids $<10^{-8}$ g are successfully eliminated after the second layer. The figure also shows the substantial damage that the fragments from a very large ($\sim$1 g) micrometeoroid can cause to each layer.

To determine the damage rate per year for a given mass, we use Eq. (39) to calculate the differential fluxes for each mass and multiply this by the damage per particle. Figure 22 shows the damage that would be caused per year for a micrometeoroid at a given mass for the 0.5 mil case. The plot indicates that micrometeoroids between the range of 10^{-8} to 10^{-4} g will be the most problematic because they have a balance between occurrence and damage caused.

The damage rates per particle size shown in Fig. 22 are integrated over to determine the total damage rate per year that would be experienced by each membrane. This corresponds to the integral term in Eq. (20). Figure 23 shows the results for film thicknesses of 0.5, 1, and 2 mil.

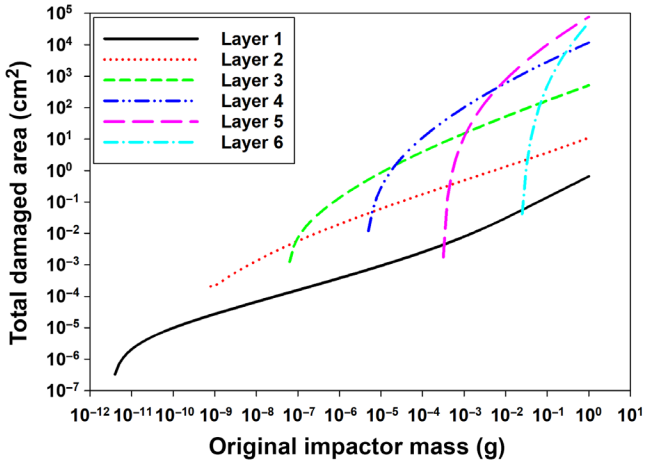

Fig. 21 Total damage due to fragments on each consecutive (0.5 mil) membrane based on the mass of the original micrometeoroid impactor. Mass is lost after each interface due to the inability of the smallest fragments to penetrate the membrane.

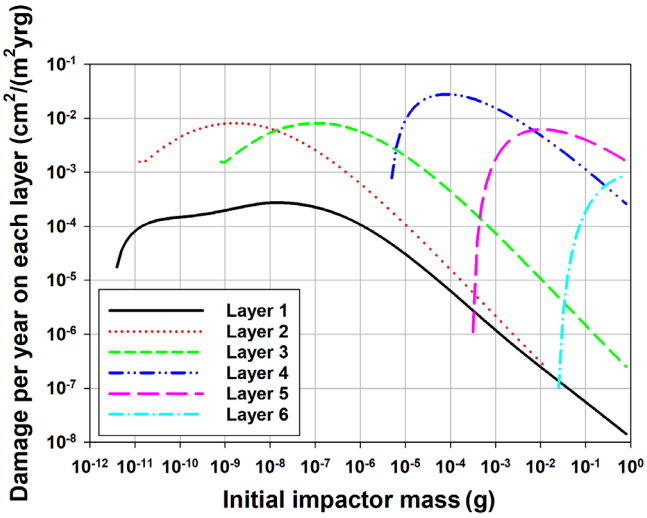

Fig. 22 Grun flux model at the 1 AU location and the damage per micrometeoroid calculated in Fig. 21 are used to estimate the damage rate on each 0.5 mil membrane for a given impacting micrometeoroid size.

The fourth and fifth layers of the micrometeoroid shield sustain the most damage. The micrometeoroid fragments are successfully eliminated after the sixth layer for a film thickness of 2 mil and after the seventh layer for film thicknesses of 0.5 and 1 mil. Therefore, adequately protecting against micrometeoroids will require several layers of Kapton sheets. However, it is worth noting that, in this analysis, the authors have assumed that the fragments maintain the impactor's original speed as a worst-case scenario to be conservative for the starting point of an initial shield design. In practice, a micrometeoroid shield may not require as many layers as that indicated by Fig. 23, but additional hypervelocity tests impacting multiple Kapton layers will need to be performed to determine what the appropriate number of layers would need to be to effectively protect an inflatable reflector.

It is worth noting that Fig. 23 can also be used to determine the damage to an unshielded lenticular: layers 1 and 2 can be thought of as the entrance and exit membranes, respectively. The authors would like to highlight the effect of a thicker membrane in the case of an unshielded lenticular: a thicker membrane has the opposite effect desired and actually increases the total damage areas A_{ent} and A_{exit} because κ is amplified at these d_p/f ratios for the incoming micrometeoroid distribution. The integral term in Eq. (20) is estimated using values from Fig. 23 for

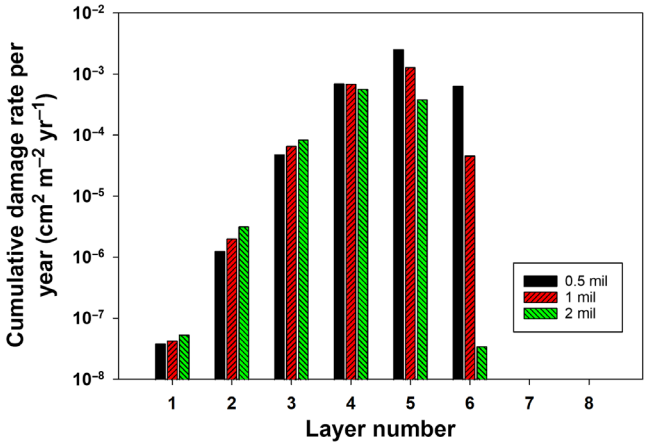

Fig. 23 Damage rate per micrometeoroid mass in Fig. 22 is integrated across all micrometeoroid masses to determine the total damage per year per m^2.

the 0.5 mil case, which results in a rate of 1.3×10^{-6} $\frac{\text{cm}^2}{\text{m}^2\text{yr}}$ near the 1 AU location. This rate is then plugged into Eq. (20) to determine the total hole area with time and subsequently to estimate the gas required to complete the mission (covered in the next section).

5 Mass Loss from Punctures and Permeation

The efficacy of the inflatable structure to operate as a primary reflector is rooted in the ability to maintain a static shape through constant pressure. This can be accomplished through a pressure maintenance system that will apply corrections to account for any changes in the number of gas molecules or temperature. We expect drops in pressure to occur as the gas escapes through tiny punctures caused by micrometeoroids, which will require the pressure maintenance system to replenish the gas. To derive a function to describe the flow rate out of the lenticular, we need to determine which regime describes the flow. In addition, we also consider the possibility of gas escaping through permeation. We use these descriptions as our basis for determining the total gas required to maintain the reflector over the course of the mission lifetime.

At a typical operating temperature and pressure for an inflatable optic of 300 K and 3.5 Pa, the mean free path for a gas will be on the order of 4 mm. Using a micrometeoroid speed of 35 km/s and computing the corresponding κ for an impact on 0.5 mil Kapton (Fig. 20), we find that the mean free path is considerably larger than the hole diameters caused by micrometeoroids for particle masses $\leq 10^{-4}$ g. Micrometeoroids greater than this mass have a low occurrence rate; therefore, the gas flow caused by the majority of punctures can be described by effusion.

The effusion regime describes the flow rate Q_{eff} out of a small hole area A_H [defined in Eq. (20)] as[12]

$$Q_{\text{eff}} = PA_H\sqrt{\frac{1}{2\pi m_{\text{molec}}k_BT}}, \tag{43}$$

where P is the gas pressure, m_{molec} is the mass per molecule, k_B is the Boltzmann constant, and T is the temperature of the gas. To get the rate of mass lost, $\dot{m} = \frac{\text{dm}}{\text{dt}}$, Q_{eff} is multiplied by the mass per molecule, m_{molec}

$$\dot{m} = Q_{\text{eff}}m_{\text{molec}} = -PA_H\sqrt{\frac{M}{2\pi N_Ak_BT}}, \tag{44}$$

where M is the molar mass, N_A is Avogadro's number, and $m_{\text{molec}} = \frac{M}{N_A}$. Note the dependence of Eq. (44) on temperature: in the format in which we wrote the equation, the mass loss rate is inversely proportional to the temperature. This means that gas escapes more slowly for hotter systems, and faster for colder systems, which initially seems counterintuitive. However, if the system maintains a constant pressure and volume, which will be imposed for an inflatable system, then the temperature increases are accompanied by a decrease in the number of molecules in the balloon, which leads to less collisions, and vice versa.

As part of the mission design, all terms in Eq. (44) remain constant, with the exception of the hole area and gas temperature. The gas temperature will have a limited range due to the sun illumination angles allowed by the mission design, and the hole area A_H will continually increase with time. Recall that the micrometeoroid hole accumulation [Eq. (20)] is proportional to the diameter of the reflector. Consequently, larger diameter designs will have significantly shorter lifetimes for the same allocated gas budget compared with their smaller diameter counterparts because they lose gas more efficiently. This results in a trade-off between aperture size and mission lifetime.

Now that we have defined the function for gas escape and the terms that it contains, we can quantify the total gas needed over a mission lifetime, Z. Substituting the equation for the hole accumulation rate A_H [Eq. (20), recall that this is described by the initial holes due to the

construction seams plus additional holes due to micrometeoroid impacts], into Eq. (44) and substituting in the gas constant, $R = N_A k_B$, we rewrite the time rate of mass loss as

$$\frac{dm}{dt} = -A_{\text{seams}} P \sqrt{\frac{M}{2\pi RT}} - A_R P \sqrt{\frac{M}{2\pi RT}} t \int_{m_{p,\min}}^{m_{p,\max}} \Phi(m_p) A_{\text{impact}} \mathrm{d}m_p. \tag{45}$$

As complicated as Eq. (45) looks, it is very simple, namely,

$$\frac{dm}{dt} = -(yt + j), \tag{46}$$

where y is given as

$$y = A_R P \sqrt{\frac{M}{2\pi RT}} \int_{m_{p,\min}}^{m_{p,\max}} \Phi(m_p) A_{\text{impact}} \mathrm{d}m_p, \tag{47}$$

and j is

$$j = A_{\text{seams}} P \sqrt{\frac{M}{2\pi RT}}, \tag{48}$$

with a bounding lower value used for T. In Eqs. (47) and (48), all of the terms are set by the mission design and are therefore known, except for the integral term in Eq. (47), which can now be approximated using our predictive model. The authors would like to highlight the implications of the dependence of dm/dt on yt in Eq. (46): because the number of holes increases linearly with time as the reflector continues to be bombarded by micrometeoroids, the resource cost to observe a target for a specified integration time becomes more and more expensive in terms of the inflatant mass as time goes on. Therefore, missions with architectures that include an intermittent inflation strategy to conserve resources and extend the overall lifetime of the mission should maximize targets with long integration times early in the mission while the mass required for replenishment is low.

The total gas mass needed for the mission is the mass needed to replace the total mass lost, given as

$$m_G = \int_0^Z (yt + j) \mathrm{d}t, \tag{49}$$

which trivially integrates to

$$m_G = \frac{y}{2} Z^2 + jZ. \tag{50}$$

As Eq. (50) clearly shows, the inflatant mass required is proportional to the square of the mission length, Z^2. The expression that we found is valid over long time scales. However, on short time scales ($\sim$1 h), there will be small deviations in the pressure (but still within the pressure tolerance of the inflatable) between corrections applied by the pressure correction system. For more information on the design of these systems, see Arenberg et al.[1].

As an example, let us calculate the gas lost due to the micrometeoroid environment for the astrophysics mission concept OASIS.[3] OASIS is a one-year mission that includes a 14 m diameter inflatable reflector located at the $L1$ Lagrange point. The lenticular is filled with neon gas at a pressure of 3.5 Pa, with typical gas temperatures of $\sim$300 K. In this thought experiment, we focus on the gas lost solely due to micrometeoroid punctures, so we set $j = 0$ in Eq. (50). In Sec. 4, we found that we can expect a total damage rate due to the full spectrum of micrometeoroids in this region to be $1.3 \times 10^{-6} \frac{\text{cm}^2}{\text{m}^2\ \text{yr}}$ [this is the integral term in Eq. (47)]. Plugging these values into Eqs. (47) and (50) gives $m_G(1\ \text{yr}) = 1.5 \times 10^{-3}$ kg. Note that the actual gas replenishment may be significantly larger than this once the seams term is included. The authors would like to remind the readers that this estimate is based on the κ extrapolation using the

observed β from the experiments; more hypervelocity impact tests are needed to refine the β parameter.

In addition to leaks caused by micrometeoroid penetrations, permeation of the pressurant gas through the reflector membrane is a second mechanism for gas loss that must be considered. The permeability of gasses through polymeric material can vary widely as a function of the permeant gas species, the membrane material, and the temperature. The permeation rate is given by Darcy's Law as

$$Q_{\text{permeation}} = K\frac{A_R}{f}\Delta P, \tag{51}$$

where $Q_{\text{permeation}}$ is the number flow rate, K is the permeability, A_R is the surface area of the reflector, f is the membrane thickness, and ΔP is the pressure differential of the permeant gas across the membrane (here simply the gas pressure within the reflector). The temperature dependence of the permeability is given as

$$K \propto \exp\left(-\frac{E_K}{k_B T}\right), \tag{52}$$

where E_K is the energy of permeation. The mass loss from the gas permeating through the reflector material over an elapsed time t is then found as

$$m_{\text{permeation}}(t) = \rho_g Q t, \tag{53}$$

where ρ_g is the mass density of the gas, which is solved using the ideal gas law as

$$\rho_g = \frac{PM}{RT}, \tag{54}$$

with M being the molar mass and R being the gas constant. Substituting this into Eq. (53) we solve for the total mass lost over the mission lifetime Z as

$$m_{\text{permeation}}(Z) = \frac{PM}{RT}QZ. \tag{55}$$

Comparing Eqs. (50) and (55), we can see that the gas loss due to holes is proportional to Z^2, whereas loss due to permeation is linearly dependent on Z.

To understand which loss mechanism will dominate, let us again examine the case for OASIS. Schowalter et al.[13] found $K = 3.1 \times 10^{-11}\ \frac{\text{cm}^3\ \text{at STP mm}}{\text{storrcm}^2}$ for neon. Plugging in the relevant numbers gives $Q_{\text{permeation}} = 2 \times 10^{-10}\ \text{m}^3/\text{s}$. This results in a $m_{\text{permeation}}(1\ \text{yr}) = 2 \times 10^{-7}$ kg, four orders of magnitude smaller than the micrometeoroid effect. Therefore, the dominant source of gas loss will be through punctures and seams.

6 Summary and Future Work

Inflatable reflectors present a unique opportunity to enable large aperture telescopes in space. However, the lifetime of their functionality will depend on the system's ability to maintain a constant shape by maintaining the pressure within the structure. In this paper, we have shown how gas loss due to micrometeoroid punctures will be the dominant loss mechanism of this life-limiting resource. We have also presented a theoretical formulation for predicting the hole damage due to a distribution of impacting fragments to better enable estimations of this gas loss rate.

Hypervelocity tests using a ruby impactor on kapton sheets indicated that a micrometeoroid will fragment with an $\alpha_f = 4$ and a $c_{\max} = 0.24$. We used these empirical values to create a predictive model for micrometeoroid impacts on a polyimide film. Using this model, we estimated that a micrometeoroid shield consisting of 6-7 layers (depending on the thickness of the

polyimide sheets) would be needed to properly mitigate the micrometeoroid environment at the 1 AU location and extend the lifetime of the inflatable optic.

More tests are needed to determine how efficiently the micrometeoroids are eliminated at each membrane barrier, refine the β parameter variation with velocity, investigate fragment elongation, and determine the effects of stand-off distance between the membranes. We have presented a prediction for future tests that incorporate multiple membranes to replicate the efficacy of a micrometeoroid shield. Comparisons of those tests to predictions can help refine the current model.

Acknowledgments

Support for this project was provided by Northrop Grumman internal funds. We would like to thank the staff at White Sands Hypervelocity Test Facility. We also would like to thank Dr. Tiffany Glassman of Northrop Grumman and our anonymous reviewers for helpful comments resulting in a more readable manuscript. A version of Sec. 5 has previously appeared in a SPIE conference proceeding: Proceedings Volume 11820, Astronomical Optics: Design, Manufacture, and Test of Space and Ground Systems III; 118200T (2022) https://doi.org/10.1117/12.2594706.

References

1. J. W. Arenberg et al., "OASIS architecture: key features," *Proc. SPIE* **11820**, 118200S (2021).
2. R. E. Freeland et al., "Large inflatable deployable antenna flight experiment results," *Acta Astron.* **41**(4–10), 267–277 (1997).
3. J. W. Arenberg et al., "Architecture of inflatable reflectors for astronomy," in preparation (2022).
4. H. Quach et al., "Surface measurement of a large inflatable reflector in cryogenic vacuum," *Photonics* **9**(1), 1 (2022).
5. D. J. Gardner, J. A. M. McDonnell, and I. Collier, "Hole growth characterisation for hypervelocity impacts in thin targets," *Int. J. Impact Eng.* **19**(7), 589–602 (1997).
6. M. J. Neish and S. Kibe, "Hypervelocity impact damage equations for Kapton multi-layered insulation and teflon second-surface mirrors," in *Proc. 3rd Eur. Conf. Space Debris*, H. Lacoste, Ed., ESA, Vol. **3** (2001).
7. J. I. Thorpe, C. Parvini, and J. M. Trigo-Rodriguez, "Detection and measurement of micrometeoroids with Lisa pathfinder," *Astron. Astrophys.* **586**, A107 (2016).
8. J. S. Mathis, W. Rumpl, and K. H. Nordsieck, "The size distribution of interstellar grains," *Astrophys. J.* **217**, 425–433 (1977).
9. A. P. Jones, A. G. G. M. Tielens, and D. J. Hollenbach, "Grain shattering in shocks: the interstellar grain size distribution," *Astrophys. J.* **469**, 740 (1996).
10. H. Hirashita and H. Kobayashi, "Evolution of dust grain size distribution by shattering in the interstellar medium: Robustness and uncertainty," *Earth, Planets Space* **65**(10), 1083–1094 (2013).
11. E. Grün et al., "Collisional balance of the meteoritic complex," *Icarus* **62**(2), 244–272 (1985).
12. R. L. Liboff, *Kinetic Theory*, Prentice-Hall (1990).
13. S. J. Schowalter, C. B. Connolly, and J. M. Doyle, "Permeability of noble gases through Kapton, butyl, nylon, and "Silver Shield"," *Nucl. Instrum. Methods Phys. Res. A* **615**(3), 267–271 (2010).

Michaela N. Villarreal is a systems engineer at Northrop Grumman working on mission concept development for astrophysics and planetary space missions. She received her bachelor's degree in planetary science from UC Berkeley and her MS degree and PhD from UCLA in geophysics and space physics. She was previously a science team affiliate of NASAs Dawn and Europa Clipper missions.

Jonathan W. Arenberg is chief mission architect for Science and Robotic Missions at Northrop Grumman Corporation. His degrees are in physics and engineering from the University of California, Los Angeles. He has contributed to the Chandra X-ray Observatory, Starshade, the James Webb Space Telescope, and the Astro 2020 strategic missions. He is widely published, was awarded 15 European and U.S. patents, and is an SPIE Fellow.

Lauren Halvonik Harris is a systems engineer in Northrop Grumman, working in the radiation effects and survivability area. She received her bachelor's degree in physics from UCLA. She was previously an accelerator engineer at RadiaBeam technologies working on the development of plasmonic niobium photocathodes for SRF gun applications in collaboration with Jefferson Lab.